nature physics

Article

https://doi.org/10.1038/s41567-023-02326-7

Programmable Heisenberg interactions between Floquet qubits

In the format provided by the authors and unedited

Supplementary Information
for "Programmable Heisenberg interactions between Floquet qubits"

Supplementary Note 1 – Experimental Setup

Figure S1 shows the cryogenic setup and electronic wiring diagrams. The superconducting quantum processor used to perform the experiment is housed in a dilution refrigerator and operates at approximately 12 mK. The wiring is separated into two sides: the input side with predominantly attenuators, and the output side with mainly circulators and amplifiers. A combination of commercial K&L and in-house infrared Eccosorb® low-pass filters are added on both sides to mitigate high-frequency noise. The sample box is protected by tri-layer shields, with the copper shield further painted with *Berkeley black* mixture consisting of STYCAST 2850FT, silica, and carbon powder. The enclosure is made light-tight using indium seals. The parametric amplifier is placed inside a separate magnetic shield, and its pump line is also connected to low-pass filters to ensure suppression of high-frequency noise.

Due to resource constraint, only four qubits are connected to external circuitry during the experiment. All the input and output signals are diverted via directional couplers and power splitters to a spectrum analyzer for calibration. The pulses used to control the qubits are generated by an arbitrary waveform generator (AWG) at 1 GSa/s and upconverted using IQ mixers in combination with a local oscillator (LO) carrier tone. DC offsets using bias tees and local phases of the signals are calibrated to null carrier leakage. These offset parameters are found numerically by minimizing the signals at the carrier frequency using active feedback via the spectrum analyzer (SA) and COBYLA optimization.

The input signals are attenuated, filtered, and DC-blocked at room temperature to reduce noise inherent to electrical components inside the AWG. 26 dB of additional attenuation is added at the outputs of the AWG to fully utilize its dynamic range. The readout pulses are upconverted in a similar fashion. The upconversion circuit wiring is shown in the left panel of Fig. S1**c**. While the qubits are manipulated via individual on-chip coplanar traces, the readout is performed in multiplexed fashion via a common bus. The microwave tones going into the fridge are checked using the SA for consistency.

The signal reflected from a readout resonator is circulated and amplified by a traveling wave parametric amplifier (TWPA) at the mixing chamber (MXC) plate, then by a high-electron-mobility-transistor (HEMT) amplifier at the 4-K plate, and finally by a room temperature amplifier before reaching the downconversion circuit. Here, an IQ mixer combines the same LO tone with the outgoing signal to produce an IF pulse that carries the information about the qubit. The measurement signal is further amplified at room temperature and goes through low-pass filters to suppress additional noise coming from the amplification. Finally, it is digitized at a rate of 1 GSa/s by an analog-to-digital converter (ADC) board attached directly to the PXI slot of the acquisition computer and demodulated via software. The downconversion circuit is shown in the right panel of Fig. S1**c**. All electronic instruments are synchronized using a rubidium atomic clock. The components used to construct the experiment are listed in Table I.

Component	Brand	Model
Dilution fridge	BlueFors	XLD
Control chassis	Keysight	PXI M9023A
AWG	Keysight	PXI M3202A
Digitizer	AlazarTech	ATS9373
LO RF source	Keysight	MXG N5183B
Spectrum analyzer	Keysight	N9320B
Frequency standard	SRS	FS725
Para. amplifier	MIT LL	TWPA
HEMT	LNF	LNC4_8C
TWPA pump	Hittite	HMC M2100
IQ mixer	Marki	MLIQ-0416
Bias-Tee	Mini-Circuits	ZX85-12G-S+
Attenuator	XMA	4882-6240
IR filter mixture	Laird	Eccosorb®CR-110

TABLE I. Component brands and models used in the experimental setup.

Supplementary Note 2 – Device Tuneup and Characterization

The device used in this experiment consists of eight single-junction transmon qubits. Each is formed by two superconducting electrodes sandwiching a thin layer of aluminum oxide, resulting in a Josephson junction with Josephson energy E_J shunted by a capacitor with charging energy E_C. These characteristic energies define the spectrum of the qubit, resembling that of an anharmonic oscillator with transition frequency between the first two levels $\omega_{01}/2\pi \approx \sqrt{8E_J E_C} - E_C$ and anharmonicity $\alpha/2\pi \approx -E_C$ [1]. They are pairwise-coupled to mutual coplanar stripline (CPS) resonators (Main Fig. 1**a**), resulting in an effective capacitive coupling [2]. These couplers are designed to have frequencies at around 7 GHz and a resonator-qubit coupling strength of approximately 70 MHz. Each qubit is coupled to a separate control line and a CPW readout resonator. All readout resonators are coupled to a common bus which also serves as a Purcell filter.

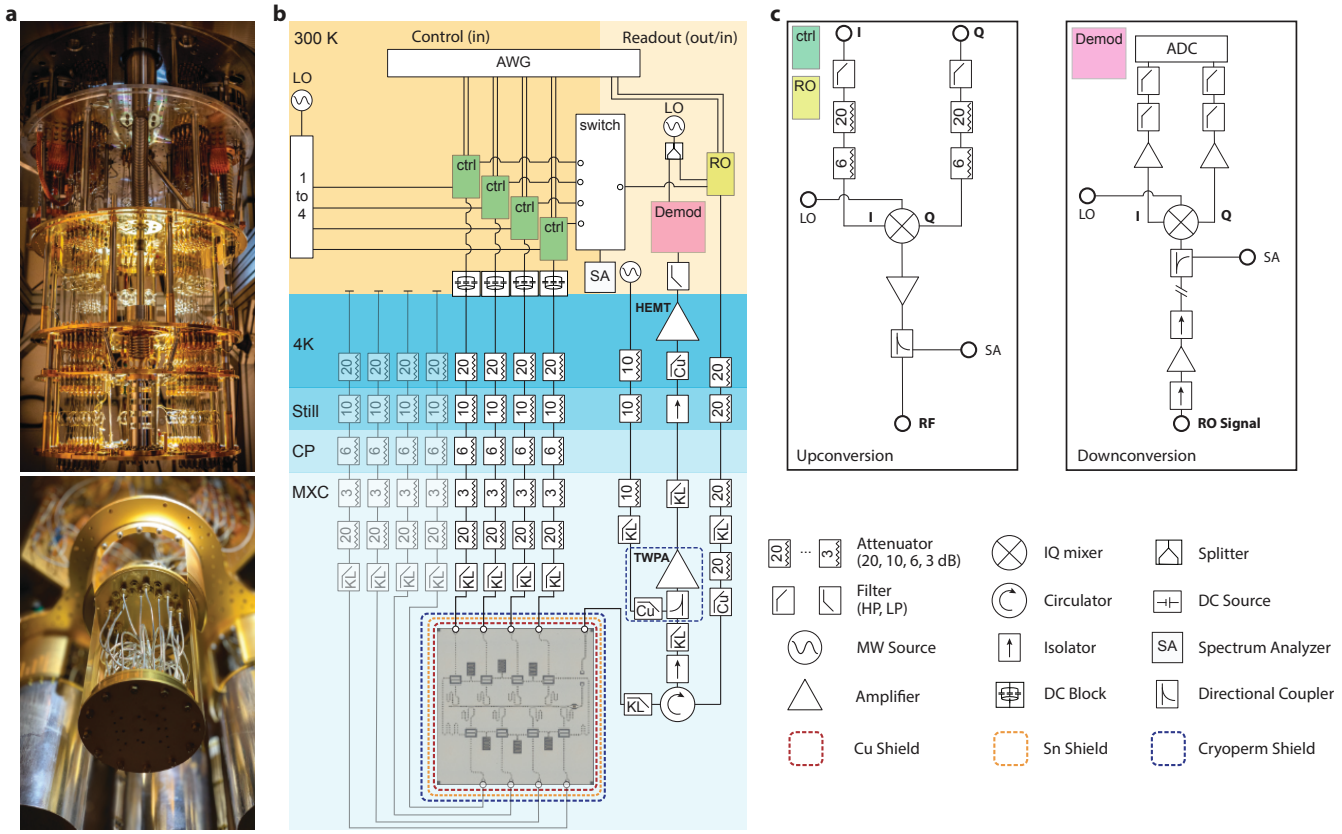

Fig. S1. **Experimental setup**. **a,** Dilution unit setup. **b,** Cryogenic wiring diagram. **c,** Room temperature control and readout circuitry.

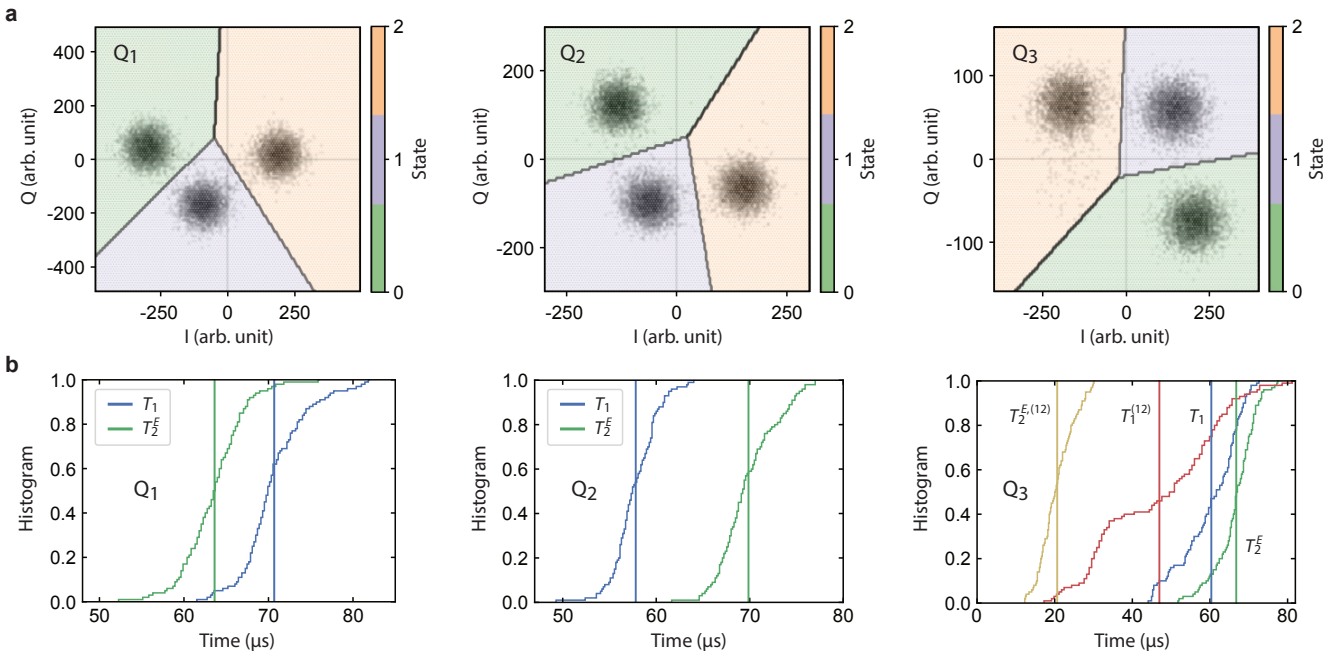

Fig. S2. **Device characterization**. **a,** Dispersive readout histogram showing the IQ signal of the resonators corresponding to the qubits in state $|0\rangle$, $|1\rangle$, and $|2\rangle$. **b,**. Coherence statistics acquired continuously for 100 iterations. The vertical lines indicate their average values.

The extracted parameters of the qubits and their readout used in this experiment are listed in Table II. The readout and qubit frequencies are measured using microwave spectroscopy. The TWPA pump tone is calibrated using a vector network analyzer to optimize the signal-to-noise-ratio. The readout pulse is set to be 1-μs long, and its amplitude is adjusted to optimize the measurement fidelity $\mathcal{F}_{\mathrm{RO}}(|i\rangle) = P(i|i)$, where $P(x|y)$ is the probability that the qubit initialized in state $|y\rangle$ is measured to be in state $|x\rangle$. The qubit-state-dependent readout signals are shown on the IQ planes in Fig. S2**a**.

The relaxation time T_1 and echo dephasing time T_2^E are extracted by applying a pulse sequence with variable length to the qubit, measuring the signal from the readout resonators, then fitting the data to appropriate functions with a decay parameter. Typical coherence time statistics consisting of ensembles of 100 individual measurements are shown in Fig. S2**b**. We also measure the coherence statistics of the $|1\rangle \leftrightarrow |2\rangle$ transition for Q_3, with $\overline{T}_1^{(12)} = 46.96$ μs and $\overline{T}_2^{E,(12)} = 20.97$ μs.

Single-qubit pulses have a Gaussian shape and are set to be 30-ns long. A series of Ramsey sequences is applied to extract the correct qubit frequencies. Their amplitudes are calibrated for $\mathrm{R_X}(\pi/2)$ pulses by repeatedly applying even numbers of them up to $n_{\mathrm{pulse}} = 200$ and measuring the outcomes to zero-in the correct parameters. By using the $\mathrm{R_X}(\pi/2)$ gate in combination with virtual-Z gates, single qubit rotations can be implemented using the ZXZXZ decomposition [3], which significantly reduces the calibration time and complexity. Single-qubit gate fidelities extracted via streamline randomized benchmarking are included in Table II.

Classical microwave crosstalk is present in the device (Table III) and degrades its performance via two distinct processes. Firstly, an off-resonant microwave tone applied to the qubit slightly dresses its resonant frequency as discussed in the main text, leading to phase errors during execution of intended quantum circuits. Secondly, a leaked microwave tone applied to one qubit at the frequency of another qubit coupled to it induces a ZX interaction, which is commonly known as the cross-resonance effect, leading to spurious entanglement between the qubits. Thus, it is important to detect and suppress such crosstalk to improve chip-scale performance. To accomplish this, additional microwave tones are applied simultaneously to neighboring qubits during the gate operation of the intended qubits. Their amplitudes and phases are tuned up to destructively interfere with the crosstalk tones. The parameters are further optimized using covariance matrix adaptation (CMA) with simultaneous randomized benchmarking. Typically, the simultaneous single-qubit gate errors are considerably higher than the isolated errors (Table II). Although we routinely observe high isolated single-qubit gate fidelities immediately following a calibration round, the simultaneous fidelities tend to saturate toward the reported numbers, which are more relevant for the present experiment.

	Q_1	Q_2	Q_3
$\omega_{01}/2\pi$ (GHz)	5.23	5.32	5.44
$\alpha/2\pi$ (GHz)	-0.26	-0.27	-0.27
$\omega_{\mathrm{RO}}/2\pi$ (GHz)	6.23	6.32	6.44
$\overline{T}_1$ (μs)	70.67	57.81	60.35
$\overline{T}_2^E$ (μs)	63.62	69.87	66.77
$\mathcal{F}_{\mathrm{RO}}$ ($\|0\rangle$)	99.6%	99.3%	99.1%
$\mathcal{F}_{\mathrm{RO}}$ ($\|1\rangle$)	98.2%	97.4%	97.5%
$\mathcal{F}_{\mathrm{RO}}$ ($\|2\rangle$)	96.8%	96.8%	95.8%
$\mathcal{F}_{\mathrm{1Q}}$ (isolated)	99.88(1)%	99.85(1)%	99.80(1)%
$\mathcal{F}_{\mathrm{1Q}}$ (joint)	99.68(1)%	99.4(1)%	99.72(3)%

TABLE II. Relevant device parameters.

	L_1	L_2	L_3
Q_1	64.72	17.45	4.22
Q_2	13.65	58.92	42.33
Q_3	11.84	21.38	53.72

TABLE III. Microwave crosstalk in the device. A fixed-amplitude microwave drive is applied to the control line L_i at the frequency of qubit Q_j, and the resulting Rabi oscillation frequency Ω_{ij} (in MHz) is extracted via dispersively measuring Q_j. The finite crosstalk then effectively manifests as $\Omega_{i\neq j} > 0$.

Using optimal readout and single-qubit gate parameters, a readout confusion matrix is extracted for each qubit by preparing it in a certain state and measuring the probability for it to be in $|0\rangle$, $|1\rangle$, or $|2\rangle$ states. This results in a matrix that is ideally diagonal with entries equal to 1. Thus, a correction matrix can be found by inverting the confusion matrix. The correction matrix is subsequently applied to all measurement outcomes to compensate for readout errors.

Supplementary Note 3 – Floquet Analysis of a Two-Level System

We consider a periodically driven qubit system described by the Hamiltonian

$$\hat{\mathcal{H}}_{\mathrm{q}}(t)/\hbar = -\frac{\omega_{\mathrm{q}}}{2}\hat{\sigma}_{\mathrm{z}} + A\cos(\omega_{\mathrm{d}}t + \varphi)\hat{\sigma}_{\mathrm{x}}. \tag{1}$$

For a coherent drive with period $T = 2\pi/\omega_{\mathrm{d}}$, we can find a time-periodic Floquet state, $|u(t)\rangle_{\mathrm{F}} = |u(t+T)\rangle_{\mathrm{F}}$, with quasienergy $\hbar\varepsilon$ through the Floquet equation,

$$\left(\hat{\mathcal{H}}_{\mathrm{q}}(t) - i\hbar\partial_t\right)|u(t)\rangle_{\mathrm{F}} = \hbar\varepsilon|u(t)\rangle_{\mathrm{F}}. \tag{2}$$

Note that this equation is connected to the Schrödinger equation via the relation $|u(t)\rangle_{\mathrm{F}} = e^{i\varepsilon t}|\psi(t)\rangle$. To find the solutions of Eq. (2), we write the Floquet state as a Fourier series comprising of time-independent states $|u^k\rangle$,

where k is an integer,

$$|u(t)\rangle_{\rm F} = \sum_k e^{ik\omega_{\rm d}t}|u^k\rangle, \tag{3}$$

and then inserting it into the Floquet equation. By grouping terms which have the same Fourier frequencies, we can obtain $\varepsilon|u^k\rangle = (-\frac{\omega_{\rm q}}{2}\hat{\sigma}_{\rm z} + k\omega_{\rm d})|u^k\rangle + e^{i\varphi}\frac{A}{2}\hat{\sigma}_{\rm x}|u^{k-1}\rangle + e^{-i\varphi}\frac{A}{2}\hat{\sigma}_{\rm x}|u^{k+1}\rangle$. Under the conditions $A \ll \omega_{\rm q}, \omega_{\rm d}$ and $\omega_{\rm q} \leq 2\omega_{\rm d}$, this can be put into the matrix form,

$$\begin{bmatrix} -\frac{\omega_{\rm q}}{2}\hat{\sigma}_{\rm z} + k\omega_{\rm d} & e^{i\varphi}\frac{A}{2}\hat{\sigma}_{\rm x} \\ e^{-i\varphi}\frac{A}{2}\hat{\sigma}_{\rm x} & -\frac{\omega_{\rm q}}{2}\hat{\sigma}_{\rm z} + (k-1)\omega_{\rm d} \end{bmatrix} \begin{bmatrix} |u^k\rangle \\ |u^{k-1}\rangle \end{bmatrix} = \varepsilon \begin{bmatrix} |u^k\rangle \\ |u^{k-1}\rangle \end{bmatrix}. \tag{4}$$

Its eigenstates yield the Floquet basis states using Eq. (3),

$$\begin{aligned} |u_+(t)\rangle_{\rm F} &\propto \left(\delta + \sqrt{A^2+\delta^2}\right)|0\rangle + e^{-i(\omega_{\rm d}t+\varphi)}A|1\rangle, \\ |u_-(t)\rangle_{\rm F} &\propto \left(\delta - \sqrt{A^2+\delta^2}\right)|0\rangle + e^{-i(\omega_{\rm d}t+\varphi)}A|1\rangle, \end{aligned} \tag{5}$$

and its eigenvalues give the quasienergies of $e^{ik\omega_{\rm d}t}|u_\pm(t)\rangle_{\rm F}$ as

$$\varepsilon_\pm^k = \left(k - \frac{1}{2}\right)\omega_{\rm d} \pm \frac{1}{2}\sqrt{A^2+\delta^2}, \tag{6}$$

where $\delta = \omega_{\rm d} - \omega_{\rm q}$ is the drive detuning. In this work, we allocate the index of the Floquet basis to match with that of the bare basis, i.e., $|\langle n|u_n(t)\rangle_{\rm F}|^2 > 0.5$. Specifically, if $\delta > 0$, we define $|u_{+(-)}(t)\rangle_{\rm F}$ as $|u_{0(1)}(t)\rangle_{\rm F}$ and $\varepsilon_{+(-)}$ as $\varepsilon_{0(1)}$, otherwise the index is inverted. Thus, the quasienergy difference, $\varepsilon_{01} \equiv \varepsilon_1 - \varepsilon_0$, abruptly changes at $\delta = 0$ (Fig. S3**a**).

Supplementary Note 4 – Floquet Analysis of a Three-Level System

We further extend the Floquet analysis to a qutrit system to explore the possible impact of the $|2\rangle$ state on the results. Since the present experiment leverages transmon qubits, which are also the workhorse in superconducting quantum computing, we proceed with a three-level system Hamiltonian inspired by this platform,

$$\begin{aligned} \hat{\mathcal{H}}_q/\hbar = &-\frac{\omega_{\rm q}}{2}|0\rangle\langle 0| + \frac{\omega_{\rm q}}{2}|1\rangle\langle 1| + (\frac{3\omega_{\rm q}}{2} + \alpha)|2\rangle\langle 2| \\ &+A\cos(\omega_{\rm d}t+\varphi)(|0\rangle\langle 1| + |1\rangle\langle 0| + \sqrt{2}|1\rangle\langle 2| + \sqrt{2}|2\rangle\langle 1|). \end{aligned} \tag{7}$$

For consistency, the drive detuning is denoted as $\delta = \omega_{\rm d} - \omega_{\rm q}$, where $\omega_{\rm q} \equiv \omega_{01}$. The drive is thereby resonant with the qutrit's $|0\rangle - |1\rangle$ and $|1\rangle - |2\rangle$ transitions at the detuning values $\delta = 0$ and $\delta = \alpha$, respectively. The analysis can be simplified when the drive amplitude $|A|$ is small compared to the anharmonicity $|\alpha|$ if the energy and state hybridization of the $|0\rangle - |1\rangle$ transition are considered as perturbed by the $|1\rangle - |2\rangle$ transition, and vice versa.

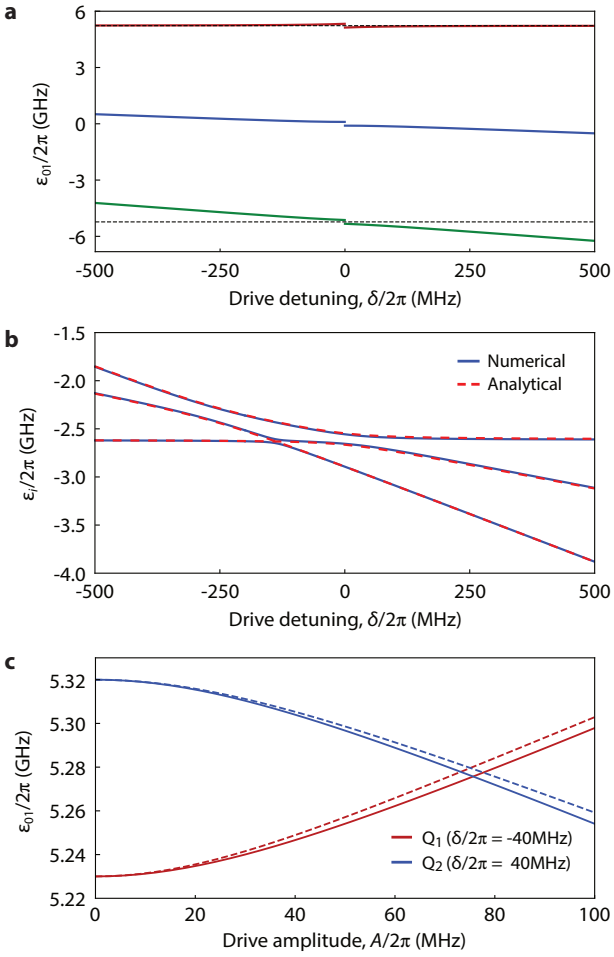

Fig. S3. **Floquet quasienergies**. **a,** Transition energies of a two-level system between $|u_0(t)\rangle_{\rm F}$ and $|u_1(t)\rangle_{\rm F}$ with drive amplitude 100 MHz. The dashed lines represent the qubit frequency of 5.23 GHz. **b,** Floquet quasienergies of three-level Q_1 with drive amplitude 100 MHz. The analytical curves correspond to ε_a^0, ε_b^0, and ε_c^{-1} in Eq. (11). **c,** Dependence of ε_{01} on the drive amplitude. By driving qubit $Q_1(Q_2)$ with red(blue) detuned microwave, two qubits can be brought into resonance. The solid and dashed lines represent the results from the two-level and three-level models, respectively. The simulation parameters of Q_1 and Q_2 are given in Table II.

From the two-level system results (Eqs. (5) and (6)), we can obtain the Floquet states relating to the $|1\rangle$ and $|2\rangle$ states around the detuning value $\delta \sim \alpha$ as

$$\begin{aligned} |\nu_+(t)\rangle_{\rm F} &\propto (\delta - \alpha + \sqrt{2A^2 + (\delta-\alpha)^2})|1\rangle \\ &\quad + e^{-i(\omega_{\rm d}t+\varphi)}\sqrt{2}A|2\rangle, \\ |\nu_-(t)\rangle_{\rm F} &\propto (\delta - \alpha - \sqrt{2A^2 + (\delta-\alpha)^2})|1\rangle \\ &\quad + e^{-i(\omega_{\rm d}t+\varphi)}\sqrt{2}A|2\rangle, \end{aligned} \tag{8}$$

and their quasienergies are given by

$$\mu_\pm^k = \left(k - \frac{1}{2}\right)\omega_{\rm d} \pm \frac{1}{2}\sqrt{2A^2 + (\delta-\alpha)^2} + \omega_{\rm q} + \frac{\alpha}{2}, \tag{9}$$

where $\omega_{\rm q}+\alpha/2$ corresponds to the average energy of $|1\rangle$ and $|2\rangle$. Then, we modify the results of the $|0\rangle-|1\rangle$ transition perturbatively using these to obtain the Floquet states of a three-level system,

$$\begin{aligned}
|u_a(t)\rangle_{\rm F} &\propto (\delta+\sqrt{A^2+\delta^2})|0\rangle + e^{-i(\omega_{\rm d}t+\varphi)}A|\nu_+(t)\rangle,\\
|u_b(t)\rangle_{\rm F} &= |u_-(t)\rangle_{\rm F},\\
|u_c(t)\rangle_{\rm F} &= |\nu_-(t)\rangle_{\rm F},
\end{aligned} \tag{10}$$

with the corresponding quasienergies

$$\begin{aligned}
\varepsilon_a^k &= \varepsilon_+^0+\mu_+^k-\frac{\omega_{\rm q}}{2},\\
\varepsilon_b^k &= \varepsilon_-^k,\\
\varepsilon_c^k &= \mu_-^k.
\end{aligned} \tag{11}$$

Here, for simplicity, we assume that the two-photon transition between $|0\rangle$ and $|2\rangle$ states around $\delta=\omega_{\rm q}/2+\alpha$ is forbidden. Consequently, we do not take into account the perturbation of $|u_-(t)\rangle_{\rm F}$ and $|\nu_-(t)\rangle_{\rm F}$. Figure S3**b** shows that the analytical solutions of three quasienergy levels agree well with the numerical simulation results. Additionally, as shown in Fig. S3**c**, we compare ε_{01} obtained from two-level and three-level models. We can deduce from this result that the discrepancy between the two models is small for moderate drive detuning and amplitude, which validates our two-level approximation assumed throughout this work.

Supplementary Note 5 – Heisenberg Interactions between Floquet States

As described by Eq. (4) in the main text, the interaction strengths of the Floquet-engineered Heisenberg Hamiltonian are given as

$$\begin{aligned}
J_{\rm XY} &= J\langle c_{01}^{(1)}c_{10}^{(2)}\rangle_t = J\langle c_{10}^{(1)}c_{01}^{(2)}\rangle_t,\\
J_{\rm ZZ} &= J\langle c_{11}^{(1)}c_{11}^{(2)}+c_{00}^{(1)}c_{00}^{(2)}-c_{00}^{(1)}c_{11}^{(2)}-c_{11}^{(1)}c_{00}^{(2)}\rangle_t,
\end{aligned} \tag{12}$$

where $c_{ab}^{(n)}=\langle\psi_a^{(n)}(t)|\hat{\sigma}_{\rm x}^{(n)}|\psi_b^{(n)}(t)\rangle$ is for qubit Q_n and $\langle\ldots\rangle_t$ denotes the time-average value. For the transverse (XY) spin-exchange interaction, we drive $\mathrm{Q}_1(\mathrm{Q}_2)$ with red(blue) detuned microwaves to bring their quasienergy differences $\varepsilon_{01}^{(n)}$ into resonance. Specifically, this condition is satisfied for quasienergy transitions $e^{ik\omega_d^{(n)}t}|u_0^{(n)}(t)\rangle_{\rm F}\leftrightarrow e^{i(k+1)\omega_d^{(n)}t}|u_1^{(n)}(t)\rangle_{\rm F}$ when mapped by a certain drive amplitude (Eq. (6) and Fig. S3**b**). Accordingly, the Floquet states' coefficients read

$$\begin{aligned}
c_{01}^{(1)} &= \langle\psi_0^{(1)}(t)|\hat{\sigma}_{\rm x}^{(1)}|\psi_1^{(1)}(t)\rangle\\
&= e^{-i\varepsilon_{01}^{(1)}t}\langle u_-^{(1)}(t)|_{\rm F}\hat{\sigma}_{\rm x}^{(1)}e^{i\omega_{\rm d}^{(1)}t}|u_+^{(1)}(t)\rangle_{\rm F}
\end{aligned} \tag{13}$$

and

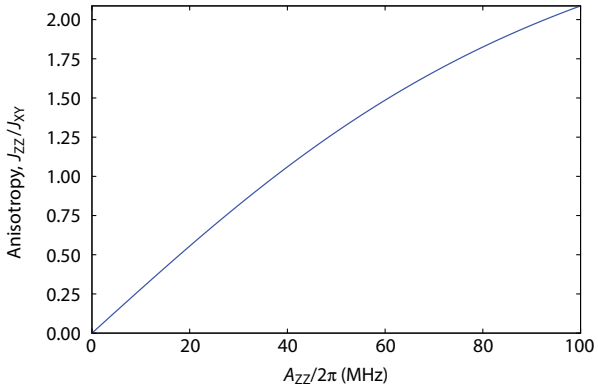

Fig. S4. **Programmable anisotropy**. Using Eqs. (15) and (18), the anisotropy $\Delta=J_{\rm ZZ}/J_{\rm XY}$ is calculated with respect to the drive amplitude $A_{\rm ZZ}$ of pulse p_3 in Main Fig. 2**a**. Here, the pulses p_1 and p_2 have the same amplitude $A_{\rm XY}/2\pi=70$ MHz, and the drive detunings are $\delta_1/2\pi=-\delta_2/2\pi=-40$ MHz. The phase difference between p_1 and p_3 is $\varphi=\varphi_3-\varphi_1=0$.

$$\begin{aligned}
c_{10}^{(2)} &= \langle\psi_1^{(2)}(t)|\hat{\sigma}_{\rm x}^{(2)}|\psi_0^{(2)}(t)\rangle\\
&= e^{i\varepsilon_{01}^{(2)}t}\langle u_-^{(2)}(t)|_{\rm F}e^{-i\omega_{\rm d}^{(2)}t}\hat{\sigma}_{\rm x}^{(2)}|u_+^{(2)}(t)\rangle_{\rm F}.
\end{aligned} \tag{14}$$

When the blue- and red-detuned drives have the same detuning $|\delta|$ and amplitude A, the time-average XY interaction strength is obtained as

$$|J_{\rm XY}| = J|\langle c_{01}^{(1)}c_{10}^{(2)}\rangle_t| = J\frac{(|\delta|+\sqrt{A^2+\delta^2})^2}{4(A^2+\delta^2)}, \tag{15}$$

using Eq. (5). On the other hand, the relevant coefficients for the longitudinal (ZZ) spin-spin interaction read

$$\begin{aligned}
c_{\pm\pm}^{(n)} &= \langle u_\pm^{(n)}(t)|_{\rm F}\hat{\sigma}_{\rm x}^{(n)}|u_\pm^{(n)}(t)\rangle_{\rm F}\\
&= \frac{A_n(\delta_n\pm\sqrt{A_n^2+\delta_n^2})\cos\left(\omega_{\rm d}^{(n)}t+\varphi_n\right)}{A_n^2+\delta_k\left(\delta_n\pm\sqrt{A_n^2+\delta_n^2}\right)}.
\end{aligned} \tag{16}$$

From the coefficient, we can estimate the time-dependent ZZ interaction strength of

$$\begin{aligned}
&c_{11}^{(1)}c_{11}^{(2)}+c_{00}^{(1)}c_{00}^{(2)}-c_{11}^{(1)}c_{00}^{(2)}-c_{00}^{(1)}c_{11}^{(2)}\\
&= c_{++}^{(1)}c_{++}^{(2)}+c_{--}^{(1)}c_{--}^{(2)}-c_{++}^{(1)}c_{--}^{(2)}-c_{--}^{(1)}c_{++}^{(2)}\\
&= \frac{4A_1A_2\cos\left(\omega_{\rm d}^{(1)}t+\varphi_1\right)\cos\left(\omega_{\rm d}^{(2)}t+\varphi_2\right)}{\sqrt{(A_1^2+\delta_1^2)(A_2^2+\delta_2^2)}}.
\end{aligned} \tag{17}$$

Especially, if we set the drive frequency of $\omega_{\rm d}^{(1)}$ and $\omega_{\rm d}^{(2)}$ to be the same, the time-averaged ZZ interaction strength is given as

$$\begin{aligned}
J_{\rm ZZ} &= J\langle c_{11}^{(1)}c_{11}^{(2)}+c_{00}^{(1)}c_{00}^{(2)}-c_{00}^{(1)}c_{11}^{(2)}-c_{11}^{(1)}c_{00}^{(2)}\rangle_t\\
&= J\frac{2A_1A_2\cos(\varphi_1-\varphi_2)}{\sqrt{(A_1^2+\delta_1^2)(A_2^2+\delta_2^2)}}.
\end{aligned} \tag{18}$$

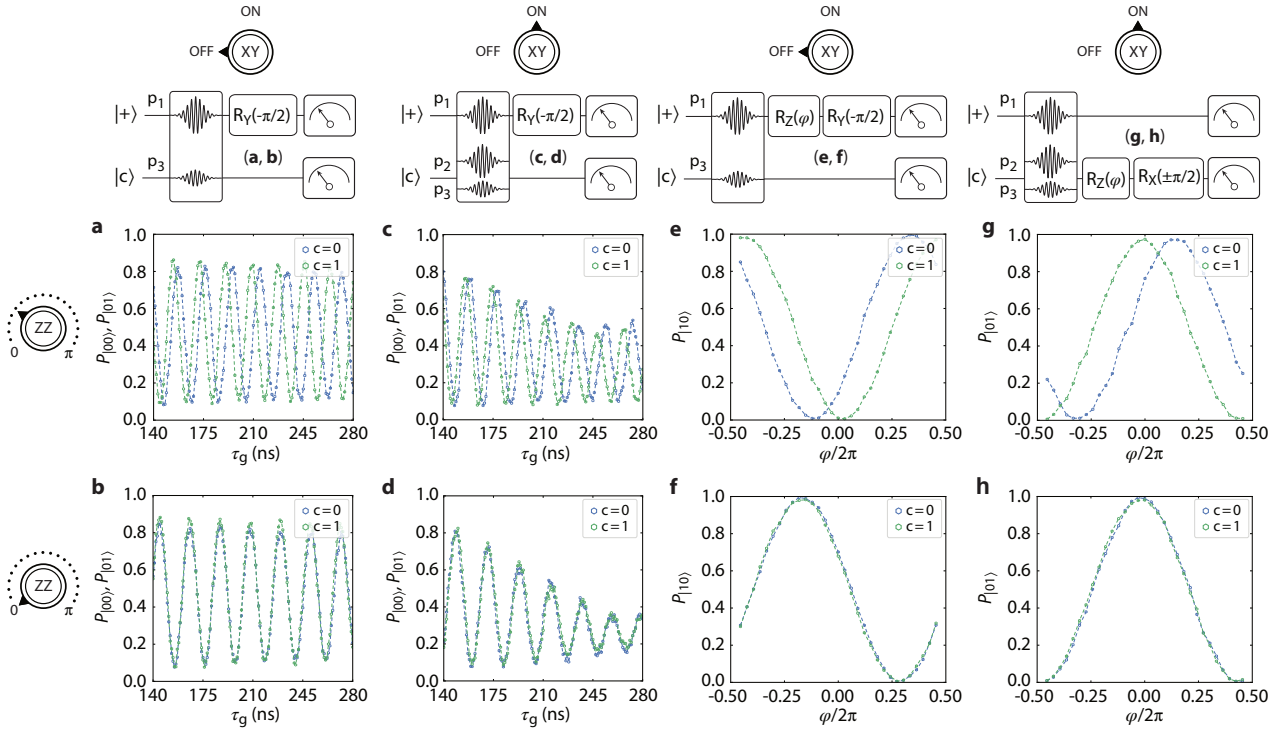

Fig. S5. **Spin-spin interaction measurement**. **a-d,** Dependence of Q_1's Z rate on Q_2's state, with transverse coupling off (**a-b**) and on (**c-d**). **e-f,** Dependence of Q_1's Z phase on Q_2's state, without transverse coupling. The phase difference results from Φ_{ZZ}. **g-h,** When the two-qubit states $|10\rangle$ and $|01\rangle$ are swapped via XY coupling, the sequence instead includes the projection gate on Q_2. The angle polarity is chosen according to the initial control state. The analysis takes into account the 2π phase difference between the curves when $\Phi_{ZZ} = 0$ to mimic the result without transverse coupling.

In the experiment, J_{XY} is enabled by pulses p_1 and p_2, while J_{ZZ} depends on p_1 and p_3. (See Main Fig. 2). To estimate the programmable range of the anisotropy $\Delta = J_{ZZ}/J_{XY}$, we compute it using Eqs. (15) and (18) with our pulse parameters. Figure S4 shows that the anisotropy can be adjusted between 0 and 2 with relatively modest amplitude A_{ZZ}, allowing a wide variety of quantum simulation applications.

Supplementary Note 6 – ZZ Interaction Measurements

The ZZ rate can be estimated using a time-efficient and reliable Ramsey-like experiment. The sequence consists of initializing one qubit in a superposition state, then applying the intended pulses and measuring it along the Z axis. The Z rotation resulting from the frame frequency difference between the bare qubit and the Floquet qubit manifests as an oscillation of the qubit's population with respect to the pulse duration. For a finite spin-spin coupling, the two oscillation frequencies corresponding to the other qubit in the ground and excited states are subtracted to find the ZZ rate. As this always works for both zero and finite XY coupling (Fig. S5**a-d**), it is a versatile method to approximate the longitudinal coupling. However, its accuracy is limited by the fast oscillations and subsequently the fitting errors.

To accurately measure the ZZ angle at the end of a pulse with a fixed duration τ_g, a sequence with the addition of a single-qubit Z gate with a variable phase φ is used. The measured qubit population depends on φ, and Φ_{ZZ} is the phase difference corresponding to the other qubit being in $|0\rangle$ and $|1\rangle$ states (Fig. S5**e-f**). The measurement also works when there is a complete population swap between $|10\rangle$ and $|01\rangle$. In this case, the Z gate is applied to the other qubit instead, with the projection gate's polarity depending on its initial state. $\Phi_{ZZ} = 0$ then corresponds to the phase difference of 2π, which can be subtracted from the results to give overlapping trajectories for zero ZZ coupling. We note that since the qubit is expected to be in the ground state if there is no phase gate induced by the pulse, a similar approach is used to calibrate single-qubit Z gates. Finally, the method can be extended to analyze a three-qubit CCZ entanglement.

For simultaneous transverse coupling resulting in arbitrary swapping angle, we find tomographic reconstruction to be the most reliable. In this approach, quantum state tomography and quantum process tomography are performed to find the state or process matrices resulting from the applied gate. An optimization routine is then utilized to extract the swapping (XY) and ZZ angles.

The accuracy of this method is inherently limited by the SPAM errors of the tomography procedures.

Supplementary Note 7 – Two-Qubit Gate Calibration

The programmable interactions can be employed to implement two-qubit gates in a straightforward manner. Since the XY and ZZ operations commute, we can decompose the Heisenberg unitary as $\hat{U}_{\mathrm{XXZ}}(\Theta_{\mathrm{XY}}, \Phi_{\mathrm{ZZ}}) = e^{-i\hat{\mathcal{H}}_{\mathrm{XXZ}}t/\hbar} = \hat{U}_{\mathrm{XY}}(\Theta_{\mathrm{XY}}) \times \hat{U}_{\mathrm{ZZ}}(\Phi_{\mathrm{ZZ}})$, where

$$\hat{U}_{\mathrm{XY}}(\Theta_{\mathrm{XY}}) = \exp\left[-i\frac{\Theta_{\mathrm{XY}}}{2}(\hat{X}\hat{X}+\hat{Y}\hat{Y})\right] = \begin{pmatrix} 1 & 0 & 0 & 0 \\ 0 & \cos(\Theta_{\mathrm{XY}}) & -i\sin(\Theta_{\mathrm{XY}}) & 0 \\ 0 & -i\sin(\Theta_{\mathrm{XY}}) & \cos(\Theta_{\mathrm{XY}}) & 0 \\ 0 & 0 & 0 & 1 \end{pmatrix} \quad (19)$$

and

$$\hat{U}_{\mathrm{ZZ}}(\Phi_{\mathrm{ZZ}}) = \exp\left[-i\frac{\Phi_{\mathrm{ZZ}}}{2}\hat{Z}\hat{Z}\right] = \begin{pmatrix} e^{-i\Phi_{\mathrm{ZZ}}/2} & 0 & 0 & 0 \\ 0 & e^{i\Phi_{\mathrm{ZZ}}/2} & 0 & 0 \\ 0 & 0 & e^{i\Phi_{\mathrm{ZZ}}/2} & 0 \\ 0 & 0 & 0 & e^{-i\Phi_{\mathrm{ZZ}}/2} \end{pmatrix}. \quad (20)$$

Naturally, the coherent flip-flop between $|10\rangle$ and $|01\rangle$ in Main Fig. 2**c** is equivalent to the rotation of the transverse coupling angle Θ_{XY}, with $\Theta_{\mathrm{XY}} = \pi/2$ corresponding to a full swap (the oscillation angle is $2\Theta_{\mathrm{XY}}$). The measured longitudinal coupling angle Φ_{ZZ} in Main Fig. 2**d** illustrates a control-phase entangling operation up to local Z rotations, with $\Phi_{\mathrm{ZZ}} = \pi/2$ corresponding to a CZ gate following the relation $\hat{U}_{\mathrm{CZ}} = \exp\left[-i\pi(\hat{Z}\hat{Z}+\hat{I}\hat{I}-\hat{Z}\hat{I}-\hat{I}\hat{Z})/4\right]$. Therefore, two-qubit gates can be calibrated up to local Z gates using the observed interactions. Notably, the realized iSWAP and SWAP gates arise directly from the XX and isotropic XXX Heisenberg models, while the CZ gate results from the pure spin-spin coupling of the transverse-field Ising model. In sum, the realized Floquet system can be used as a robust quantum many-body simulator with high-fidelity gates as consequences.

With the connection between different interaction models and gate unitaries established, the presented gates are calibrated as follows. (i) First, a frequency sweep using a large-amplitude microwave pulse is performed to exclude spectrally crowded regions (See Fig. S12**b**) (ii) The pulses are applied at the appropriate frequencies, with p_1 and p_2 facilitating the transverse coupling, while p_1 and p_3 inducing the longitudinal coupling. (iii) A complete swap angle $\Theta_{\mathrm{XY}} = \pi/2$ and zero ZZ angle, $\Phi_{\mathrm{ZZ}} = 0$, (cf. Main Fig. 2) correspond to an iSWAP gate, up to local Z gates. The measurement can be performed with the intended gate repeated for an odd number of times, amplifying coherent errors, to find the correct pulse parameters. (iv) With p_2 off, there is no transverse coupling, and p_3 can be tuned to get $\Phi_{\mathrm{ZZ}} = \pi/2$, giving the CZ gate. (v) With p_1 and p_2 calibrated to give a complete population swap, p_3 can be tuned to get $\Phi_{\mathrm{ZZ}} = \pi/2$, giving the SWAP gate. (vi) The local phase gates are implemented in software by tracking the frame of the qubit and imparting relative phases on subsequent single-qubit pulses. Their angles are calibrated via least square optimization using tomographic measurement of the final states. Using these calibration steps, we realized a 230-ns-long iSWAP gate with $\{A_1, A_2, A_3\}/2\pi = \{71.7, 65.2, 21.35\}$ MHz, a 180-ns-long CZ gate with $\{A_1, A_3\}/2\pi = \{71.2, 28.5\}$ MHz, and a 260-ns-long SWAP gate with $\{A_1, A_2, A_3\}/2\pi = \{96.9, 28.5, 14.2\}$ MHz. As Q_3's $|1\rangle \leftrightarrow |2\rangle$ frequency is close to that of Q_1's $|0\rangle \leftrightarrow |1\rangle$, we implemented the CZ gate by applying p_1 and p_3 at a frequency 40 MHz blue-detuned from Q_1 to avoid any spectator leakage error. The qubits' population in each state is measured after mapping back to the bare basis to check for nonadiabaticity, including leakage to higher levels, which can be viewed as nonadiabatic effect involving those levels.

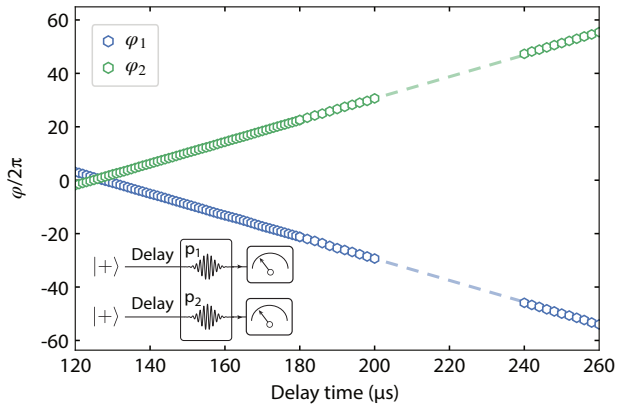

Fig. S6. **Dynamical phase accumulation**. After preparing the qubits in the superposition state $(|0\rangle+|1\rangle)\otimes(|0\rangle+|1\rangle)/2$, calibrated pulses are employed to facilitate $|10\rangle$ and $|01\rangle$ coherent exchange (inset). Tomographic measurement reveals the qubits' Z phases which are linearly dependent on the time at which the swap pulses are applied.

Supplementary Note 8 – Dynamical Phase and Z Gates

In general, integrating a gate resulting from the transverse coupling into a quantum circuit must overcome two technical requirements. First, while the XY interaction is facilitated between the Floquet qubits in the dressed

frame, the measurements and single-qubit gates are performed on the bare qubits with different transition frequencies. This leads to an accumulation of single-qubit phases that depend on the time at which the gate is applied, and the accumulation rate is equal to the difference in qubit frequencies [4]. To verify this effect, we apply pulses p_1 and p_2 calibrated to implement a perfect swap, then measure the local Z phases $\varphi_{1,2}$ of the qubits. Upon sweeping the delay time before applying the pulses, we find these phases to increase linearly, and the extracted slope is, within measurement uncertainty, the same as the qubits' frequency difference, as shown in Fig. S6. Including other gates before this transverse swap has the same effect (gap between the data points). Thus, the Z gate corrections must take this dynamics into account.

Second, the ZXZXZ single-qubit gate decomposition using virtual-Z gates comes with the following caveats. This scheme realizes arbitrary single-qubit rotation via Euler decomposition [3],

$$\begin{aligned}\hat{U}(\theta,\phi,\lambda) &= \hat{\mathrm{R}}_{\mathrm{Z}}(\phi)\hat{\mathrm{R}}_{\mathrm{X}}(\theta)\hat{\mathrm{R}}_{\mathrm{Z}}(\lambda) \\ &= \hat{\mathrm{R}}_{\mathrm{Z}}\left(\phi-\frac{\pi}{2}\right)\hat{\mathrm{R}}_{\mathrm{X}}\left(\frac{\pi}{2}\right)\hat{\mathrm{R}}_{\mathrm{Z}}(\pi-\theta)\hat{\mathrm{R}}_{\mathrm{X}}\left(\frac{\pi}{2}\right)\hat{\mathrm{R}}_{\mathrm{Z}}\left(\lambda-\frac{\pi}{2}\right).\end{aligned} \tag{21}$$

Here, the Z rotation is implemented virtually by keeping track of all the physical single-qubit X gates and redefining the rotation axes for all the gates following an intended Z gate, a procedure known as *phase carrying*. A compatible two-qubit unitary must therefore be a *phase carrier*. This procedure thus breaks down when there is an energy exchange gate in the circuit, for instance, $\sqrt{\mathrm{iSWAP}}$. In addition, since $\hat{X}\hat{X}$ and $\hat{Y}\hat{Y}$ do not commute with single-qubit $\hat{Z}$, it is problematic to implement virtual-Z gates in the circuit to correct for the additional single-qubit Z phases induced during the operations [5].

In this work, we utilize the special property of the swap angle $\Theta_{\mathrm{XY}} = \pi/2$, $(\hat{\mathrm{R}}_{\mathrm{Z}}(\varphi_1)\otimes\hat{\mathrm{R}}_{\mathrm{Z}}(\varphi_2))\times\hat{U}_{\mathrm{XXZ}}(\pi/2,\Phi_{\mathrm{ZZ}}) = \hat{U}_{\mathrm{XXZ}}(\pi/2,\Phi_{\mathrm{ZZ}})\times(\hat{\mathrm{R}}_{\mathrm{Z}}(\varphi_2)\otimes\hat{\mathrm{R}}_{\mathrm{Z}}(\varphi_1))$, to compile the quantum circuits. The induced Z phases occured during the gate operations can also be corrected by applying virtual-Z gates afterward [4]. The circuit compilation thus requires two additional steps at each iSWAP or SWAP cycle, which can be satisfied by computing and adding virtual-Z gates after them: (i) correction gates for Z phases must account for the dynamical phase accumulation due to the frame difference, and (ii) the phase tracking for virtual-Z gates must switch the frames. In practice, condition (i) only requires accounting for the time interval between consecutive gates, and condition (ii) is fulfilled by adding/subtracting the carrying phase, which is an internal part of the compilation software. We note that SU(2) compilations that are compatible with any two-qubit gate have been recently introduced [5], so other gates in the XY family are in principle fully compatible with any platform supporting native virtual-Z gates.

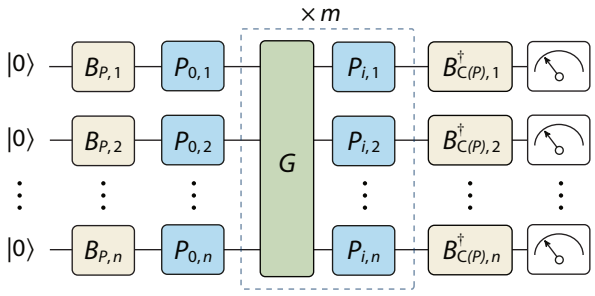

Fig. S7. **Cycle benchmarking sequence**. The sequence consists of a cycle of preparation gates B_P, followed by a cycle of Pauli gate P. The gate of interest G is interleaved between cycles of randomly-sampled Pauli gates for m different iterations. Finally, the qubits are rotated to the original eigenstates via a cycle of $B^{\dagger}_{C(P)}$'s. A reference sequence has the identity gate replacing the G cycle.

Supplementary Note 9 – Cycle Benchmarking

Cycle benchmarking (CB) [6] is a scalable benchmarking protocol for characterizing errors and noise in cycles containing parallel gate operations. Unlike randomized benchmarking (RB), which tailors all errors into a global depolarizing channel via Clifford twirling, CB tailors all errors into stochastic Pauli channels via Pauli twirling. To measure the errors for a Pauli channel $P \in \{I,X,Y,Z\}^{\otimes n}$ for a cycle of operations containing n qubits, the register of qubits is first prepared in an eigenstate of P via single-qubit basis operations B_P, followed by a cycle of randomly-sampled Pauli gates P, after which the cycle or gate of interest G is interleaved between alternating cycles of randomly-sampled Pauli gates for m iterations, and finally the register of qubits is rotated back to the eigenstate of P via refocusing gates $B^{\dagger}_{C(P)}$. Each Pauli channel P is fitted to an exponential decay function $A_P f_P^m$ for a circuit depth m using Levenberg-Marquardt algorithm, where the fidelity of each Pauli channel,

$$f_P = \mathrm{Tr}\Big[C(P)^{\dagger}\tilde{C}(\rho)\Big], \tag{22}$$

is captured by the overlap of the results of the ideal circuit $C(P)$ with the noisy implementation $\tilde{C}(\rho)$, where ρ represents the initial state of the n-qubit system in a $+1$-eigenstate of P; the constant A_P represents the state preparation and measurement (SPAM) error. By measuring the performance of the interleaved gate cycle G at two different circuit depths $\{m_1, m_2\}$ for K different Pauli channels, one may estimate the process fidelity via

$$\mathcal{F}_{\mathrm{p}} = \frac{1}{K}\sum_{P\in\mathbb{P}}\left(\frac{\sum_{l=1}^{L} f_{P,m_2,l}}{\sum_{l=1}^{L} f_{P,m_1,l}}\right)^{\frac{1}{m_2-m_1}}, \tag{23}$$

where $\sum_{l=1}^{L}$ represents the sum over the L different randomizations for each Pauli channel P, and $\frac{1}{K}\sum_{P\in\mathbb{P}}$ rep-

resents the average over all measured Pauli channels. Here, $\mathbb{P}$ is a subset of the n-qubit Pauli group that has been sampled from the full set of 4^n possible channels. The number of different Pauli channels $K = |\mathbb{P}| \leq 4^n$ sets the precision of the fidelity estimate [6]. The process infidelity is given as $e_{\rm p} = 1 - \mathcal{F}_{\rm p}$. Similarly, the average uncertainty is computed from the individual fitting uncertainties as $r_p = \sqrt{\sum_i^{4^n}(r_i^2)}/4^n$.

Much like interleaved RB (IRB), which measures the fidelity of a dressed gate composed of the interleaved gate G with a cycle of random Clifford gates, CB measures the fidelity of a dressed cycle composed of the interleaved cycle G and a cycle of random Pauli gates. Similar to IRB, one can estimate the average gate infidelity of just the interleaved cycle G by taking the ratio of the process fidelities of the dressed D and reference R cycles,

$$e_{\rm g} = \frac{d-1}{d}\left(1 - \frac{\mathcal{F}_{\rm p}^D}{\mathcal{F}_{\rm p}^R}\right), \tag{24}$$

where $d = 2^n$ is the dimension of the Hilbert space for n qubits. It should be noted that estimating the isolated gate fidelity via IRB or CB can be subjected to large systematic bounds, with upper and lower bounds that may differ by orders of magnitude depending on the unitarity of the gate or cycle [7]. However, it has been shown that CB tightens the upper- and lower-bounds on the fidelity estimate relative to IRB [8], due to the fact that random Pauli gates are more efficiently decomposed into native operations than random Clifford gates. Nevertheless, the twirling over either Pauli, Clifford, or Haar-random does not change the process fidelity of a gate, and previous works have shown that CB results agree well with IRB[8] and XEB [9, 10] within their uncertainties. In addition, we note that since the conditions of the qubits, including coherence times, naturally fluctuate, while the cycles of interest are not measured simultaneously, Eq. (24) should be viewed as an estimation.

Supplementary Note 10 – Cross-Entropy Benchmarking

Cross-Entropy Benchmarking (XEB) [11] is an additional SPAM-free method we leverage for studying the errors and noise associated with the three-qubit CCZ gate. XEB benefits from being able to benchmark non-Clifford unitaries and was instrumental in the first experimental demonstration of quantum advantage. In the XEB protocol, the errors of a multi-qubit gate are tailored into a global depolarizing channel via interleaved cycles of randomly chosen local $SU(2)$ gates. Given sufficient tailoring of the noise, one expects to observe scrambling behavior that manifests as the distribution of probabilities p for observing a particular bitstring following the Porter-Thomas distribution $P(p) = (d-1)(1-p)^{d-2}$, where $d = 2^n$ is the dimension of the measured Hilbert space. For a sufficiently randomized circuit, the circuit error can be conveniently thought of as the deviation of the measured bitstring distributions from a uniform distribution.

We seek to make this relationship precise. We denote all possible bitstrings as x_i for $i = 1, ..., 2^n$ where n is the number of qubits that the unitary of interest act on. We assign $q(x_i)$ as the measured distribution, and define the linear cross-entropy between two probability distributions $p_1(x)$ and $p_2(x)$ as

$$H(p_1, p_2) = \sum_x p_1(x)p_2(x), \tag{25}$$

where the sum runs over the full support of the probability distributions. The XEB circuit fidelity is then given as

$$\mathcal{F}_{\rm XEB} = \frac{H(p,q) - H(p,u)}{H(p,p) - H(p,u)} \equiv \frac{m_U - u_U}{e_U - u_U}, \tag{26}$$

where $u(x) = 1/d$ is the uniform probability distribution on the bitstrings. This expression can be understood as the difference in the ideal to measured and ideal to uniform cross entropies, normalized by the difference if the measured distribution was to perfectly match the ideal distribution (i.e. $p(x_i) = q(x_i)$ for all i).

An additional feature of the XEB routine is that at each depth m in the XEB circuits, the so-called speckle purity γ can be used to estimate the decoherence-limited cycle fidelity. It is calculated using the measured bitstring probability distributions as

$$\gamma(m) = {\rm Var}(p_m)\frac{d^2(d+1)}{(d-1)}. \tag{27}$$

Here p_m is the measured probability distribution for bitstrings at depth m in our XEB circuits, where ${\rm Var}(p_m) = (d-1)/d^2(d+1)$ for ideal pure states.

Supplementary Note 11 – Extended Gate Verification

Two-qubit gates: The implemented unitaries are also benchmarked using quantum process tomography (QPT), which can be used to approximate the residual coherent errors. For example, single-qubit Z gates can be approximated using the extracted Pauli transfer matrix (PTM) $\mathcal{R}$ using Nelder-Mead least square optimization. The PTMs for the realized gates are shown in Fig. S8**a-c**. They can be reverted using the ideal PTMs to find the error PTMs $\mathcal{R}_{\rm error} = \mathcal{R}_{\rm exp}\mathcal{R}_{\rm ideal}^{-1}$, which is useful in prescribing the residual errors to Pauli channels (Fig. S8**d-f**). The process fidelity $\mathcal{F}_{\rm p}$ and gate fidelity $\mathcal{F}_{\rm g}$ are extracted following $\mathcal{F}_{\rm p} = {\rm Tr}(\mathcal{R}_{\rm ideal}^T\mathcal{R}_{\rm exp})/d^2$

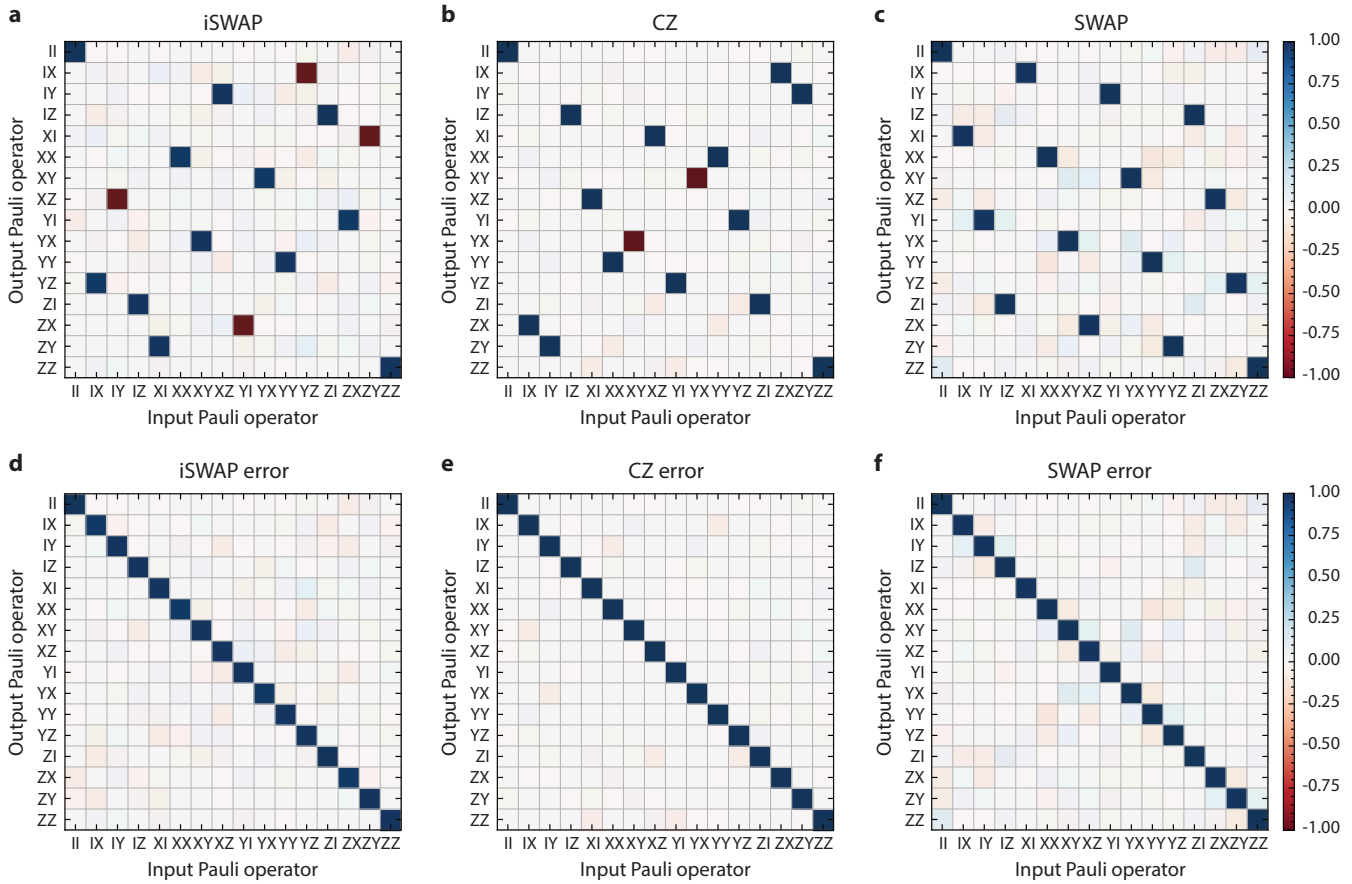

Fig. S8. **Quantum process tomography results**. Experimentally obtained PTM's corresponding to **a,** iSWAP, **b,** CZ, and **c,** SWAP gates. Their ideal counterparts are used to compute the respective error PTMs (panels **d**-**f**).

and $\mathcal{F}_g = (d\mathcal{F}_p + 1)/(d + 1)$, where $d = 4$ is the dimension of the two-qubit system. For the displayed iSWAP, CZ, and SWAP PTMs, the extracted gate fidelities are 98.4%, 99.8%, and 98.9%, respectively. Since the extracted PTMs are sensitive to SPAM errors and maximum-likelihood estimation, the fidelities should only be viewed as rough approximation, and their best utilization is for calibration.

CCZ gate: To gauge the stability of the calibration, we continuously monitor the dressed cycle fidelity over 30 consecutive iterations taking over eight hours using CB (Fig. S9**a**). Although the sequence consists of multiple gates, we only observe a small variation in the fidelity which does not break the limits imposed by coherence time fluctuations. We additionally verify the gate fidelity using cross-entropy benchmarking (XEB), achieving an average XEB fidelity of 93.3(2)% (Fig. S9**b,c**), consistent with the CB result. Note that this fidelity includes the error from single-qubit gates used to construct random cycles. XEB also allows us to extract the speckle purity, which is shown to be approximately the same as the cycle fidelity (Fig. S9**c**). This implies that the gate is coherence-limited.

The truth table is a useful tool to quickly gauge the quality of the gate. However, we observe that it is not sensitive to the residual ZZ-type interactions involving the control qubits. Therefore, we further include the truth table data with Q_2 and Q_3 as the targets (Fig. S9**d,e**), with corresponding fidelities $\mathcal{F}_{tt}$ equal to 95.95(7)% and 95.62(7)%, respectively. The spurious correlated errors must be cancelled for them to be accurate. We note that the fidelity formula presented in Refs. [12, 13] is utilized here for the convenient comparison with relevant works. Notably, the truth table fidelity results, which include SPAM errors, are better than the dressed cycle fidelity measured using CB/XEB, but comparable to the gate fidelity extracted using the reference cycle in CB. In our previous report [9], the truth table fidelity was computed using $\mathcal{F}_{tt} = [\mathrm{Tr}(\mathcal{U}_{exp}\mathcal{U}_{ideal}^{\dagger})/8]^2$. Applying it here gives the truth table fidelities equal to 92.5(1)%, 92.1(1)%, and 91.5(1)% for Q_1, Q_2, and Q_3 as target qubits, respectively. These are comparable to the dressed cycle fidelity. Shot noise introduces the uncertainty and was estimated through 1000 Monte Carlo simulation runs.

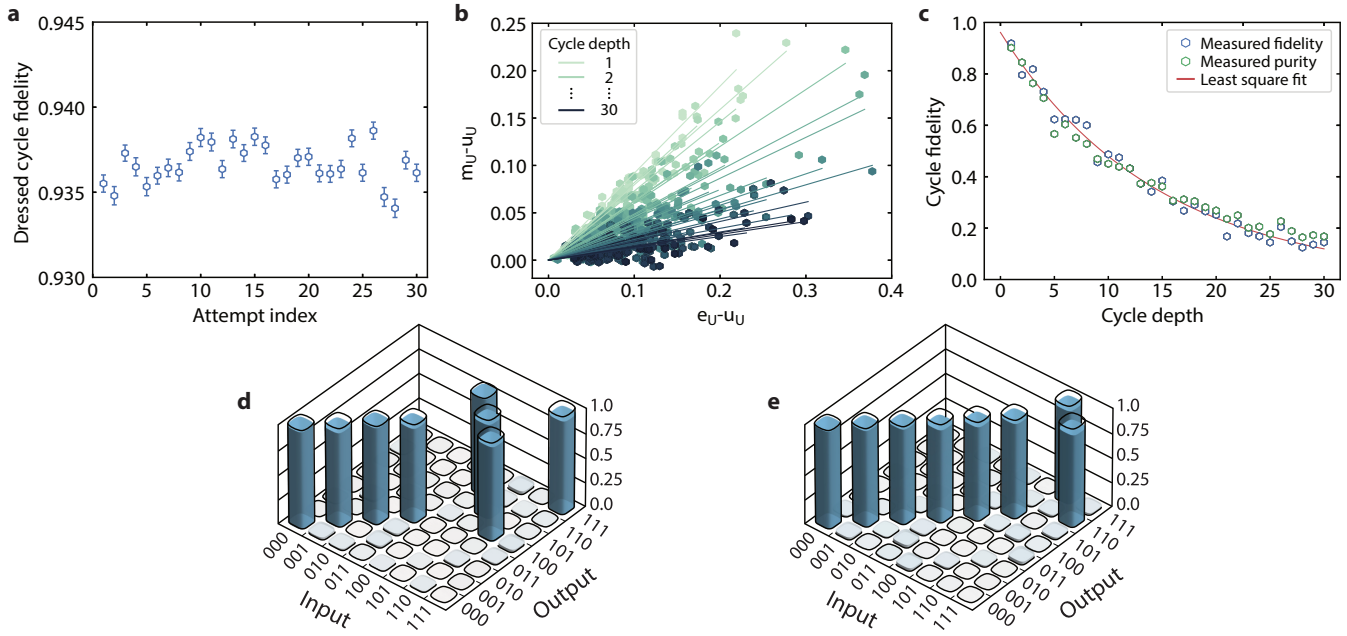

Fig. S9. **Extended verification of CCZ. a,** Fluctuation of the dressed process fidelity given by CB over a time span of eight hours. Each data point is obtained by performing a full CB measurement and fitting to the error model, and the error bar corresponds to the standard deviation. **b,** XEB circuit fidelity at different cycle depths. **c,** The overall decrease of the average XEB circuit fidelity at larger depths reveals the estimated dressed process fidelity of 93.3(2)%. Note that these fidelities include the errors from single-qubit gates used to construct random cycles. We additionally extract the speckle purity at each cycle depth, which is close to the cycle fidelity. **d,** Truth table of the Toffoli gate with Q_2 as the target. The corresponding fidelity is $\mathcal{F}_{\rm tt} = 95.95(7)\%$. **e,** Truth table of the Toffoli gate with Q_3 as the target. The corresponding fidelity is $\mathcal{F}_{\rm tt} = 95.62(7)\%$.

Supplementary Note 12 – Error Budgets

To estimate the dephasing-limited fidelity, we first assume that the qubit decays at a rate Γ_1 and dephases at a rate Γ_2, where these rates are related to the relaxation time T_1 and decoherence time T_2 as $\Gamma_1 = 1/T_1$, $\Gamma_2 = 1/T_2$. A Pauli transfer matrix (PTM) of a single-qubit decoherence channel for a duration τ is given as

$$\mathcal{E}(\tau) = \begin{pmatrix} 1 & 0 & 0 & 0 \\ 0 & e^{-\Gamma_2\tau} & 0 & 0 \\ 0 & 0 & e^{-\Gamma_2\tau} & 0 \\ 0 & 0 & 0 & e^{-\Gamma_1\tau} \end{pmatrix}. \tag{28}$$

In the absence of non-Markovian errors such as leakage and crosstalk, the PTM of a Pauli-twirled n-qubit channel is simply given by the tensor product $\mathcal{E}^{\otimes n}$. The process fidelity limited by decoherence can thus be written as

$$\begin{aligned} \mathcal{F}_{\rm p} &= \frac{1}{4^n}{\rm Tr}[\mathcal{E}^{\otimes n}] \\ &= \frac{1}{4^n}\prod_{i=1}^{n}\left(1 + e^{-\Gamma_1^{(i)}\tau} + 2e^{-\Gamma_2^{(i)}\tau}\right), \end{aligned} \tag{29}$$

where $\Gamma_1^{(i)}$ and $\Gamma_2^{(i)}$ denote the energy relaxation and dephasing rates of qubit i, respectively.

Using Eq. (29), we estimate the coherence-limited fidelities using the best undriven T_1 and T_2^E times for the upper bound, and the worst dynamical values for the lower bound. The lower fidelity bounds for iSWAP, CZ, SWAP, and CCZ gates are {99.2%, 99.4%, 99.1%, 95.1%} and the upper bounds are {99.6%, 99.7%, 99.5%, 97.1%}. Although this approach only gives approximate limits, they are already remarkably close to the obtained fidelities. We note that the CCZ sequence contains four different pulses involving different qubit pairs, so it is difficult to choose the appropriate coherence times for the analysis. However, the speckle purity measurement (Fig. S9**c**) reveals that it should be dephasing-limited. In addition, we leverage our high-fidelity qutrit readout to verify that there is no unwanted leakage/nonadiabaticity, within measurement uncertainty, at the end of all the gates.

In practice, the ramp times (∼50-100 ns) constitute a majority of the pulses used for the gates (∼200 ns), as opposed to the long pulses with mostly fixed amplitudes used in the dynamical coherence measurements (Fig. 3**b**). Besides, different gates require different combinations of pulse amplitudes and ramp times, making it challenging to systematically select the right coherence values for our approximation. Therefore, we believe that it is reasonable to estimate the fidelity limits using the presented approach. A more rigorous estimation may ideally in-

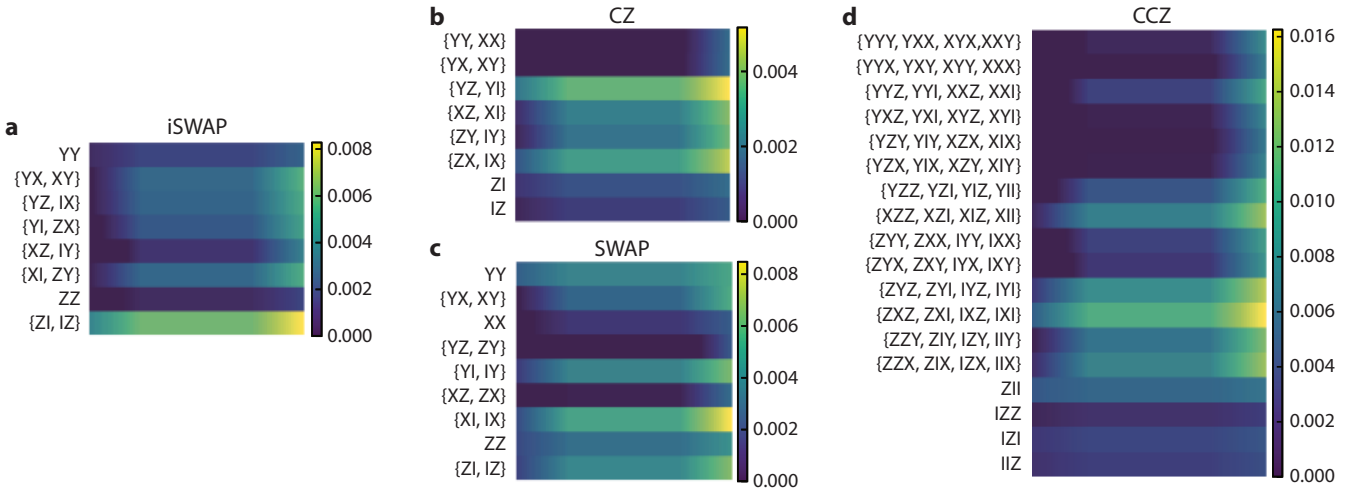

Fig. S10. **Error classification**. Pauli noise reconstruction (PNR) results showing the dominant errors impacting **a,** iSWAP, **b,** CZ, **c,** SWAP, and **d,** CCZ gates. The y-axes label the most dominant Pauli Kraus errors for each gate, the cell color denotes the error rate, and the cell gradient defines the 95% confidence interval uncertainty. Pauli errors grouped in curly brackets denote degenerate gate errors which cannot be distinguished due to the effect of the gate itself.

volve a numerical Floquet simulation with the integration of a time-dependent mapping. Future research to elucidate such dynamics, shedding light on the dephasing process, will help establish the required techniques to study spurious effects associated with Floquet-engineered interactions.

To reconstruct the dominant error channels impacting the iSWAP, CZ, SWAP, and CCZ gates, we utilize Pauli noise reconstruction (PNR) [14], also referred to as cycle error reconstruction [15]. PNR reconstructs the Pauli Kraus errors affecting each gate from a set of CB measurements (see the Supplemental Material of Ref. [15] for a detailed discussion). For example, in Fig. S10, we observe that the dominant error channel for the iSWAP gate is a Z error on either qubit, even though ZZ appears to be largely suppressed (note that IZ and ZI cannot be distinguished, due to the fact that the iSWAP gate transforms one into the other). For the CZ gate, we observe that Y-type errors on Q_1 or X-type errors on Q_2 are the most dominant. The SWAP gate is mostly affected by X- or Z-type errors on either qubit. While the error generators for the CCZ are more difficult to interpret, we consistently observe that Z-type errors on Q_1, X- or Y-type errors on Q_2, and Z-type errors on Q_3 are the most dominant.

Supplementary Note 13 – Dressed Heating and Dephasing

We utilize the single-shot readout capability of the measurement setup (cf. Fig. S2**a**) to selectively measure the dynamics of Q_1 under the drive. To measure the relaxation process, the qubit is first prepared in state $|1\rangle$ by applying a π pulse to a pre-selected $|0\rangle$ state. Then, a microwave pulse with variable amplitude and duration is applied to the qubit. The ramp time is chosen to be 100 ns to ensure adiabaticity for the amplitude values shown. We discard the data in which small oscillation appears, which correspond to the nonadiabatic regime. The qubit is measured dispersively after the off-resonant pulse, and then post-selected in the $|0\rangle$ state. The excitation dynamics is measured in a similar fashion, with the qubit prepared in the ground state and post-selected in the $|1\rangle$ state. For T_2^E, a π pulse on the undriven qubit is inserted between two Floquet drive pulses with the same ramp and duration times. This refocusing pulse is orthogonal in phase to the $\pi/2$ projection pulses. To ensure the passive reset of the qubit, a delay time of 50 μs is added between neighboring sequences.

To verify that the reduction in the obtained T_2^E times is not due to nonadiabatic effects, we repeat the measurements with different ramp times τ_r and DRAG coefficients λ_{DRAG}, and still observe a consistent decrease with respect to the pulse amplitude, as shown in Fig. S11**a**. Intriguingly, we also find a consistent heating effect that increases the excited state population after the mapping, suggesting a change in the effective qubit temperature. Notably, although the population of the qubit increases monotonically with respect to the drive amplitude (Fig. S11**b**), the extracted relaxation and excitation rates do not show any obvious trend (Main Fig. 3**b**).

We simulate this effect numerically by projecting the decoherence mechanisms onto the Floquet basis. Using the experimentally obtained ratio $\nu = P_{|1\rangle}^{\mathrm{final}}/P_{|0\rangle}^{\mathrm{final}} = 0.027$ of the undriven qubit in equilibrium (355 μs after initialization), we assume a finite relaxation rate $\Gamma_\downarrow = (T_1)^{-1}/(1+\nu)$, excitation rate $\Gamma_\uparrow = (T_1)^{-1} - \Gamma_\downarrow$, and

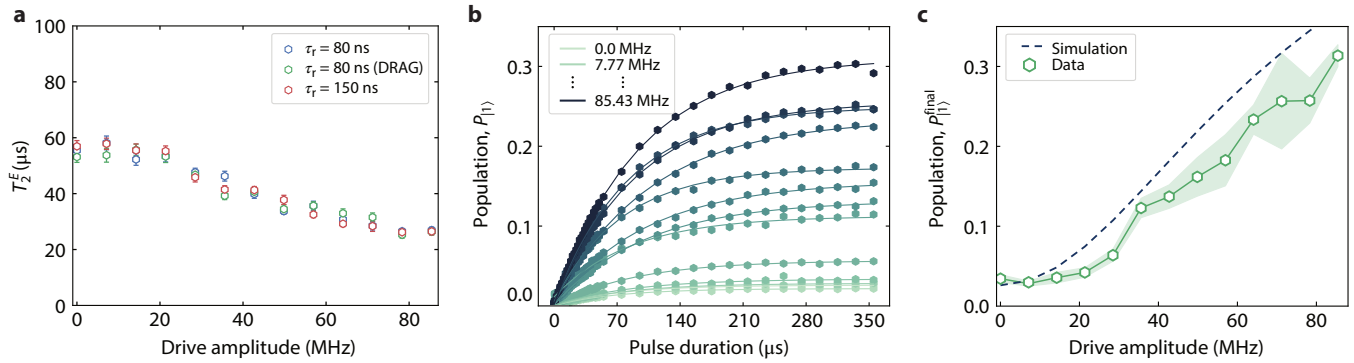

Fig. S11. **Dressed decoherence**. **a,** Dependence of Q_1's echo time T_2^E on the drive amplitude and pulse shape. Each data point is obtained by averaging an ensemble of 1024 echo measurements and fitting to an exponential function. The error bars represent the least-square fitting uncertainty, corresponding to the standard error of the mean (SEM). **b,** Q_1's excited state population after the mapping using a pulse with parametrized amplitude and duration. The qubit is first initialized in $|0\rangle$. **c,** Comparison between obtained excited state populations after a 355-μs-long pulse at various driving amplitudes (green markers, see Main Fig. 3**b**, inset) and numerically simulated values (blue dashed line).

pure dephasing rate $\Gamma_\phi = (T_2^E)^{-1} - (2T_1)^{-1}$, where T_1 and T_2^E are taken from Table II. Next, we simply map the jump operators $\hat{L}_- = \sqrt{\Gamma_\downarrow}|0\rangle\langle 1|$, $\hat{L}_+ = \sqrt{\Gamma_\uparrow}|1\rangle\langle 0|$, and $\hat{L}_\phi = \sqrt{\Gamma_\phi/2}\hat{\sigma}_z$ onto the Floquet basis, then evolve the system starting from the ground state using the Lindblad master equation. The result shown in Fig. S11**c** agrees well with the experimentally obtained data (previously shown in the inset of Main Fig. 3**b**).

Supplementary Note 14 – CCZ Gate Calibration

Three different gates must be calibrated for the CCZ sequence: (i) a $|11\rangle_c \leftrightarrow |02\rangle_c$ iSWAP gate between Q_2 and Q_3 that does not induce any spectator ZZ error between Q_1 and Q_2, (ii) a CZ gate between Q_1 and Q_2 that does not induce any spectator error, as this can lead to an effective ZZ entanglement after the shelving for control state $|11\rangle_c$, and (iii) a CPhase gate at the end to ensure an overall identity operation on Q_2 and Q_3, which must not induce extraneous ZZ between Q_1 and Q_2. We tune up these gates as follows.

Similar to XY gates between the computational levels, a frequency sweep is performed to find an appropriate detuning from Q_3's $|1\rangle \leftrightarrow |2\rangle$ transition. A single drive tone is then applied to Q_3 at this frequency, its duration and amplitude are varied until a good $|11\rangle_c \leftrightarrow |02\rangle_c$ chevron pattern is observed. The ZZ angle between Q_1 and Q_2 is measured at the end of the pulse and then cancelled by applying an additional pulse on Q_1. It is important to completely cancel this spurious coupling, since its presence results in a non-zero ZZ phase between Q_1 and Q_2 for the control state $|11\rangle_c$, rendering the shelving scheme ineffective. We found the best detuning to be 22 MHz below Q_3's $|1\rangle \leftrightarrow |2\rangle$ transition, and optimal pulse duration to be 280 ns with a ramping time of 120 ns. Similarly, a pulse on Q_3 is added during the CZ gate operation on Q_1 and Q_2 to null any spurious effect on the shelved state. To satisfy the more stringent requirements, we increase the ramping time to 90 ns and gate time to 210 ns.

After applying three pulses consecutively, the residual conditional phase Φ_{ZZ} between Q_2 and Q_3 is measured. We then apply a CPhase gate between them to invert this conditional phase, and at the same time cancel the residual ZZ coupling between Q_1 and Q_2. To satisfy the requirements, the gate consists of three microwave pulses applied to all three qubits. The pulses on Q_2 and Q_3 are tuned up first to negate all the entanglement between them. Then, the remaining ZZ phase between Q_1 and Q_2 is cancelled by applying a small-amplitude pulse to Q_1. The tuned up CPhase gate is 180-ns long, with a ramp time of 80-ns, bringing the total sequence duration to 950-ns. The calibration is performed manually in this simple fashion, so we expect even better gate performance with future optimization.

Supplementary Note 15 – Extensibility

Having shown the robustness and versatility of the Floquet protocol using a small-scale testbed, we hereby explore its extensibility to large-scale devices based on transmon and fluxonium qubits to motivate future developments using the Floquet framework. First, we demonstrate that there is a broad range of allowable qubit-qubit detuning and drive frequency. Then, we discuss the specific spectral arrangement for chain-type and square-lattice topologies. As the frequency allocation for a CZ gate implemented using off-resonant driving has already been explored [16, 17], we focus on the requirements for the iSWAP gate here.

Detuning. To demonstrate the broad range of allow-

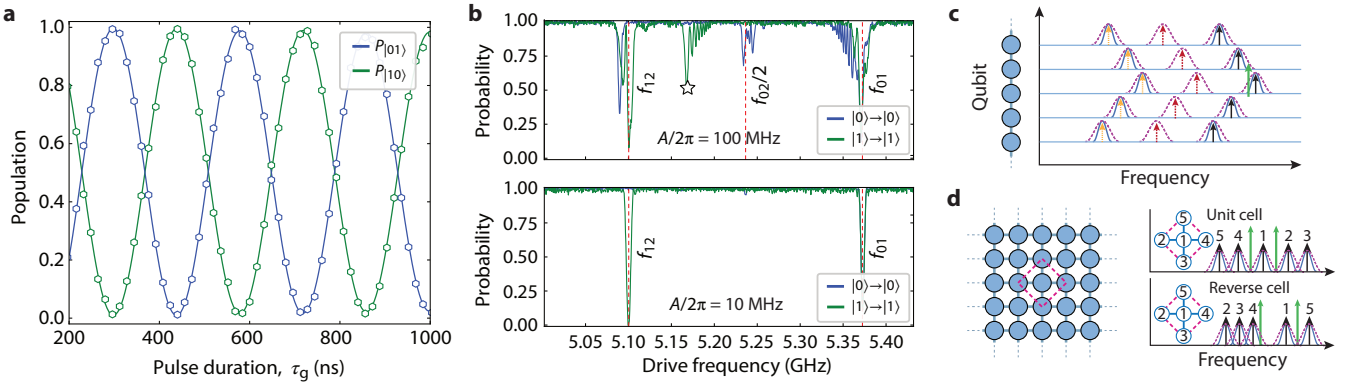

Fig. S12. **Effects of strong drives and extensibility**. **a,** Coherent flip-flop between $|10\rangle$ and $|01\rangle$ states enabled via the resonance between the Floquet qubit Q_1 and bare qubit Q_2. **b,** Potential adverse effects on a qubit under strong driving (top panel). Besides single-qubit transitions, the drive also induces a two-qubit two-photon transition, marked by ☆. The drive may also affect a neighboring qubit via the finite microwave crosstalk, which is emulated using a weak pulse (bottom panel). **c,** Arrangement of qubits in a line and their frequency allocation to allow XY interactions. The arrows represent the frequencies at which $|0\rangle \rightarrow |1\rangle$ (↑), $|1\rangle \rightarrow |2\rangle$ (↑), and $|0\rangle \rightarrow |2\rangle$ (↑) transitions are activated. The ∧ spreads represent the *adiabaticity* regions. The ∧ spreads represent the *addressability* and crosstalk-*adiabaticity* regions (see text). When two coupled-neighbors are detuned from a qubit in the same direction, the frequency at which the swap occurs is marked by the green arrow. Assuming only nearest-neighbor couplings, the arrangement can be extended to much longer chains by alternating the direction of the frequency graph. For fluxonium qubits prepared at their half-flux quantum biases, we can effectively ignore the $|1\rangle \rightarrow |2\rangle$ (↑) and $|0\rangle \rightarrow |2\rangle$ (↑) components [16]. **d,** Square-lattice arrangement and possible spectral allocation, which, for simplicity, consists only of their $|0\rangle \rightarrow |1\rangle$ frequencies. If only nearest-neighbor qubits are coupled, then we can choose the frequencies (green arrows) at which the middle qubit interacts with its neighbors without crossing other qubits' $|0\rangle \rightarrow |1\rangle$ frequencies. Typical distributions in a unit cell and in a reverse cell with Q_5 as the boundary qubit are shown. The conditions in these cells can be used to numerically optimize the frequency allocation in larger-scale devices [17].

able qubit-qubit detuning, we map Q_1 to its Floquet basis using p_1, and by tailoring the pulse, bring its quasi-frequency to match that of Q_2, which is in the bare basis. By ensuring the adiabaticity condition (using $\tau_r = 100$ ns), we observe a coherent population swapping between the qubits (Fig. S12**a**). This implies that an XY interaction can be realized between levels with detuning as high as $2 \times |\omega_1 - \omega_2| \approx 180$ MHz when both pulses are applied to map the qubits. For far-detuned transmon qubits, we can utilize their finite anharmonicity to our advantage by mapping the computational states to higher levels that have lower detuning. For example, if Q_1 and Q_2 have frequencies $\omega_1/2\pi = 5.5$ GHz and $\omega_2/2\pi = 5.7$ GHz, with the same anharmonicity of $\alpha/2\pi = -270$ MHz, then $|10\rangle$ is detuned from $|01\rangle$ by 200 MHz, while $|11\rangle$ is detuned from $|02\rangle$ by 70 MHz. Thus, it is more favorable to map $|10\rangle \rightarrow |11\rangle$, $|01\rangle \rightarrow |02\rangle$, perform the desired XY-type gate between $|11\rangle$ and $|02\rangle$, and then map the states back to effectively perform that operation between the computational states. Such a mapping scheme will not only extends the allowable qubit-qubit detuning for gate implementations but may also leverage the finite anharmonicity to overcome frequency crowding in the future.

Drive frequency. To find the spectral regions that allow the strong off-resonant driving of a qubit without violating adiabatic conditions, we apply a strong microwave pulse with amplitude $A/2\pi$=100 MHz to this qubit and measure the probability that the computational states are unchanged afterward, $P(|0\rangle \rightarrow |0\rangle)$ and $P(|1\rangle \rightarrow |1\rangle)$. As shown in Fig. S12**b**, top panel, there is a wide frequency range close to f_{01} and f_{12} where the pulse does not cause any observable nonadiabatic effect. Notably, the regions we need to avoid include those around a single-qubit two-photon transition at $f_{02}/2$ and a two-qubit two-photon excitation that leads to the transition $|01\rangle \rightarrow |12\rangle$ (marked by ☆), where the qubit being driven is Q_2 in the ket $|Q_1Q_2\rangle$ (starting from its $|1\rangle$ state). We confirm this effect by leveraging the high-fidelity readout to observe the population transfer, and then validate the effect via numerical simulation with the same driving amplitude and crosstalk. Using this analytical model, we verify that the phenomenon primarily stems from the classical microwave crosstalk in our device (Table III), so we expect this transition to be suppressed in well-designed devices with negated crosstalk. Meanwhile, such dynamics can be employed as a useful quantum tool for fixed-frequency qubits in the future.

To characterize potential adverse effects that the drive may have on neighboring qubits, we first assume that the indirect driving from crosstalk in a well-designed device is at the level ∼10% of the direct driving. Consequently, by sweeping the same microwave tone at a reduced amplitude $A/2\pi = 10$ MHz, we found the only regions to avoid to be within the proximity of f_{01} and f_{12} (Fig. S12**b**, bottom panel). Repeating these measurements on the other

qubits in our device yields similar outcomes. Therefore, we believe that there is a wide margin for the off-resonant driving condition, even in large-scale devices. It has been shown that the freedom in choosing the drive frequency should lead to better scalability in fixed-frequency transmon [17] and fluxonium architectures [16].

Chain-type connection. For near-term quantum simulation applications, devices that emulate spin-chain interactions are sufficient to explore interesting dynamics [18–20]. Thus, we first explore this type of arrangement. In addition to the general addressability requirements [17], the iSWAP gate involves shifting the Floquet qubit(s) frequencies across a wide spectral range, potentially leading to a collision with other transitions nearby. In our device and across various platforms, only nearest-neighbor qubits are coupled, so we first assume this condition. Then, the frequency arrangement may take the form of a ladder, as shown in Fig. S12**c**, which can be reversed and extended to longer arrays of qubits. Here, (i) the allocated qubit frequencies (represented as arrows, ↑ for f_{01}, ↑ for f_{12}, and ↑ for $f_{02}/2$) must be outside of the nearest neighbors' ⋀ regions to ensure addressability (a spread of ∼20 MHz), while (ii) the Floquet tones (not shown) must be applied outside of the ⩚ regions of the driven qubit (a spread of ∼40 MHz) and the ⋀ regions of neighboring qubits to ensure adiabaticity. For any qubit having neighbors that are both detuned below or above, the frequency at which the XY-interaction occurs must be located between this qubit and the neighbor with a smaller detuning (marked by the tall green arrow in Fig. S12**c**). For fluxonium qubits biased at half-integer flux quantum, we can modify this description by removing the $|1\rangle \to |2\rangle$ and $|0\rangle \to |2\rangle$ frequency components, thanks to their large anharmonicity.

Lattice-type connection. Next, we consider the connection of qubits in a dense square lattice. For simple conceptualization, we only visualize a scheme involving the $|0\rangle \to |1\rangle$ transition in Fig. S12**d**, while future works shall take into account other transitions and possible mapping protocols arising from the low anharmonicity of the transmons. Again, we assume only nearest-neighbor couplings between the qubits, which are represented by the solid lines in the lattice. We consider two types of cells (pink square): (i) a typical unit cell where the qubit at the center also has its frequency in the middle of the others', and (ii) a reverse cell where a boundary qubit is at the maximum (or minimum) allowable frequency. Similar to the chain-type connection above, we have to allocate the frequencies at which the resonant condition occurs. These are indicated by the green arrows. Using the center qubit (Q_1) as the starting point, we can then assign the frequencies of the others around it with the addressability constraint satisfied (⋀ regions do not overlap with qubit frequencies). Due to spectral crowding, to readily apply the Floquet drives to Q_1 at both red- and blue-detunings, its ⩚ region should not overlap with its neighbors' ⋀ regions. To shift the Floquet frequencies of Q_4 and Q_5 when a microwave crosstalk between them is present, the Floquet drives should be applied at a frequency ≥40 MHz red-detuned from Q_5. To mitigate direct crosstalk, we may allocate spectrally-close qubits to be physically far apart. These unit cell arrangement can be tiled and extended to optimize the arrangement in large-scale devices [17].

Allocating the frequency at which an iSWAP gate can be realized between two adjacent qubits without spurious interactions with other neighbors, in addition to arranging the qubit frequencies, becomes a challenge in devices with high connectivity, making this gate less practical than the CZ gate. A solution to this problem in the field of superconducting circuits is using a tunable coupler to control the coupling between the qubits dynamically. An architecture with Floquet qubits and tunable coupling can be considered the fixed-frequency analog of tunable-qubits with tunable coupling [21]. Here, the qubit-qubit coupling is controlled by the coupler, while the gates are implemented by the Floquet protocol as described. In this way, individual qubit-qubit coupling strengths can be easily tuned, facilitating interesting many-body quantum simulations [18–20, 22–25]. Therefore, we anticipate rapid research and development efforts in this direction to improve the performance of superconducting quantum processors. Meanwhile, small-scale or low-connectivity fixed-coupling platforms should perform well in proof-of-concept experiments, including near-term analog quantum simulation.

Supplementary Note 16 – Single-Qubit Gate in the Floquet Basis

We demonstrate the local rotation of the Floquet qubit in the dressed basis using an additional microwave drive as follows. First, we determine its frequency using a modified Ramsey sequence, with the qubit being driven during the wait time between the preparation and measurement pulses. By applying the Floquet drive with varying duration τ_g at a frequency ω_d detuned from the qubit prepared in the $|+\rangle$ state, we can extract the Ramsey fringes. The oscillation frequency (Fig. S13**a**) is then used to compute the frequency ω_F of the Floquet qubit defined by the same drive. Here, a ramp time $\tau_r = 100$ ns is used, and subsequently the pulse duration satisfies $\tau_g \geq 200$ ns.

Following the outline from Ref. [26], the Floquet qubit can be manipulated by applying an additional resonant pulse p_F at frequency ω_F during the Floquet drive at frequency ω_d. We note that this simple approach is only valid if ω_F remains constant during the control pulse. Therefore, p_F must be applied within the flat portion of the Floquet drive (Fig. S13**b**, top panel). With the duration of the pulse fixed at 50 ns, we vary its amplitude A_F, which rotates the Floquet states $|u_0\rangle$ and $|u_1\rangle$. They are

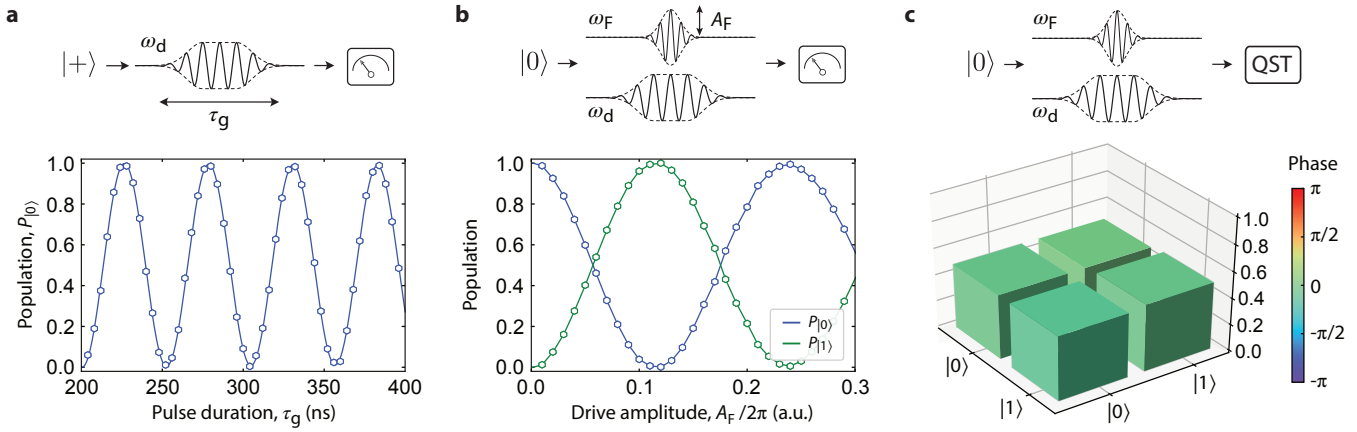

Fig. S13. **Rotation of the Floquet qubit**. **a,**. A Ramsey measurement is used to determine the frequency of the Floquet qubit. The Floquet drive is applied at a frequency $\omega_d = \omega_q + \delta$ to a qubit prepared in the $|+\rangle$ state, and then measured along the X-axis at various pulse duration τ_g, which allows us to extract the frequency shift. **b,** By applying a cosine pulse with amplitude A_F on the dressed qubit at the shifted frequency ω_F, we can rotate the states $|u_0\rangle$ and $|u_1\rangle$, which are then mapped back to the $|0\rangle$ and $|1\rangle$ states, respectively, resulting in their oscillation with respect to A_F. **c,** By choosing the correct drive amplitude A_F, we prepare the Floquet superposition state $(|u_0\rangle + e^{i\phi_F}|u_1\rangle)/\sqrt{2}$. It can then be mapped to the $|+\rangle$ state in the lab frame using local Z gate, which we confirmed via quantum state tomography.

then mapped back to the bare states $|0\rangle$ and $|1\rangle$, respectively. As shown in the bottom panel of Fig. S13**b**, we can effectively manipulate the Floquet states by varying A_F.

We proceed by choosing an amplitude A_F corresponding to $P_{|u_0\rangle} = P_{|u_1\rangle}$ (or equivalently, $P_{|0\rangle} = P_{|1\rangle}$ in Fig. S13**b**). With the high-fidelity mapping between the Floquet states and the bare states, we can perform quantum state tomography on the dressed state by measuring the bare qubit. The result shows that this pulse prepares a superposition state $(|u_0\rangle + e^{i\phi_F}|u_1\rangle)/\sqrt{2}$, which can then be mapped to the $|+\rangle$ state in the lab frame using local Z operation (Fig. S13**c**). This serves as the proof that Floquet qubits can be controlled using the same techniques developed for bare qubits. Therefore, we expect the Floquet concepts to be widely adapted for the development of novel quantum technologies in the future.

[1] J. Koch *et al.*, Phys. Rev. A **76**, 042319 (2007).
[2] J. Majer *et al.*, Nature **449**, 443 (2007).
[3] D. C. McKay, C. J. Wood, S. Sheldon, J. M. Chow, and J. M. Gambetta, Phys. Rev. A **96**, 022330 (2017).
[4] D. M. Abrams, N. Didier, B. R. Johnson, M. P. d. Silva, and C. A. Ryan, Nat. Electron. **3**, 744 (2020).
[5] J. Chen, D. Ding, C. Huang, and Q. Ye, Phys. Rev. Res. **5**, L022031 (2023).
[6] A. Erhard *et al.*, Nat. Commun. **10**, 5347 (2019).
[7] A. Carignan-Dugas, J. J. Wallman, and J. Emerson, New J. Phys. **21**, 053016 (2019).
[8] B. K. Mitchell *et al.*, Phys. Rev. Lett. **127**, 200502 (2021).
[9] Y. Kim *et al.*, Nat. Phys. **18**, 783 (2022).
[10] N. Goss *et al.*, Nat. Commun. **13**, 7481 (2022).
[11] F. Arute *et al.*, Nature **574**, 505 (2019).
[12] A. Fedorov, L. Steffen, M. Baur, M. P. da Silva, and A. Wallraff, Nature **481**, 170 (2012).
[13] J. Chu *et al.*, Nat. Phys. **19**, 126 (2023).
[14] S. T. Flammia and J. J. Wallman, ACM Trans. Quantum Comput. **1**, 3 (2020).
[15] A. Hashim *et al.*, Phys. Rev. X **11**, 041039 (2021).
[16] L. B. Nguyen *et al.*, PRX Quantum **3**, 037001 (2022).
[17] A. Morvan, L. Chen, J. M. Larson, D. I. Santiago, and I. Siddiqi, Phys. Rev. Res. **4**, 023079 (2022).
[18] Y. Salathé *et al.*, Phys. Rev. X **5**, 021027 (2015).
[19] P. N. Jepsen, J. Amato-Grill, I. Dimitrova, W. W. Ho, E. Demler, and W. Ketterle, Nature **588**, 403 (2020).
[20] A. Morvan *et al.*, Nature **612**, 240 (2022).
[21] B. Foxen *et al.*, Phys. Rev. Lett. **125**, 120504 (2020).
[22] L. Savary and L. Balents, Rep. Prog. Phys. **80**, 016502 (2016).
[23] H. Bernien *et al.*, Nature **551**, 579 (2017).
[24] J. Zhang *et al.*, Nature **543**, 217 (2017).
[25] P. N. Jepsen, Y. K. Lee, H. Lin, I. Dimitrova, Y. Margalit, W. W. Ho, and W. Ketterle, Nat. Phys. **18**, 899 (2022).
[26] A. Gandon, C. Le Calonnec, R. Shillito, A. Petrescu, and A. Blais, Phys. Rev. Appl. **17**, 064006 (2022).